NUREG/CR-1790
ORNL/NUREG/TM-416
Dist. Category R7

Contract No. W-7405-eng-26

Engineering Technology Division

LMFBR AEROSOL RELEASE AND TRANSPORT PROGRAM QUARTERLY PROGRESS REPORT FOR JANUARY–MARCH 1980

T. S. Kress M. L. Tobias

Manuscript Completed – November 24, 1980
Date Published – December 1980

Prepared for the
U.S. Nuclear Regulatory Commission
Office of Nuclear Regulatory Research
Under Interagency Agreements DOE 40-551-75 and 40-552-75

NRC FIN No. B0121

Prepared by the
OAK RIDGE NATIONAL LABORATORY
Oak Ridge, Tennessee 37830
operated by
UNION CARBIDE CORPORATION
for the
DEPARTMENT OF ENERGY

CONTENTS

FOREWORD

This report summarizes progress under the Aerosol Release and Transport (ART) Program [sponsored by the Division of Reactor Safety Research of the Nuclear Regulatory Commission (NRC)] for the period January–March 1980.

Work on this program was initially reported as Volume III of a four-volume series entitled *Quarterly Progress Report on Reactor Safety Programs Sponsored by the NRC Division of Reactor Safety Research*. Prior reports of this series are

Report No.	Period covered
ORNL/TM-4655	April–June 1974
ORNL/TM-4729	July–September 1974
ORNL/TM-4805	October–December 1974
ORNL/TM-4914	January–March 1975
ORNL/TM-5021	April–June 1975

Beginning with the report covering the period July September 1975, work under this program is now being reported as *LMFBR Aerosol Release and Transport Program Quarterly Progress Report*. Prior reports under this title are

Report No.	Period covered
ORNL/NUREG/TM-8	July–September 1975
ORNL/NUREG/TM-9	October–December 1975
ORNL/NUREG/TM-35	January–March 1976
ORNL/NUREG/TM-59	April–June 1976
ORNL/NUREG/TM-75	July–September 1976
ORNL/NUREG/TM-90	October–December 1976
ORNL/NUREG/TM-113	January–March 1977
ORNL/NUREG/TM-142	April–June 1977
ORNL/NUREG/TM-173	July–September 1977
ORNL/NUREG/TM-193	October–December 1977
ORNL/NUREG/TM-213	January–March 1978
ORNL/NUREG/TM-244	April–June 1978
ORNL/NUREG/TM-276	July–September 1978
ORNL/NUREG/TM-318	October–December 1978
ORNL/NUREG/TM-329	January–March 1979
ORNL/NUREG/TM-354	April–June 1979
ORNL/NUREG/TM-376	July–September 1979
ORNL/NUREG/TM-391	October–December 1979

Copies of all these reports are available from the Technical Information Center, Oak Ridge, Tennessee 37830.

SUMMARY

M. L. Tobias

The Aerosol Release and Transport (ART) Program at Oak Ridge National Laboratory (ORNL) is designed to investigate the release, transport, and behavior of radionuclides originating from severe accidents resulting in core melting. The experimental program is being conducted in the Fuel Aerosol Simulant Test (FAST) Facility (which also includes the CRI-III vessel), the Nuclear Safety Pilot Plant (NSPP) Facility, and the Containment Research Installation-II (CRI-II) Facility. The analytical effort is designed to support the experiments and to provide an independent assessment of the safety margins that exist for the assessment of the radiological consequences of a core meltdown accident.

During this quarter, eight underwater capacitor discharge vaporization (CDV) tests were performed in the FAST Facility; in addition, ten tests were performed in the CRI-III Facility. In the FAST tests, two water heights were used, and the water temperature varied between 298 and 364 K. Xenon pressure in the test sample was essentially zero in one case and 0.513 MPa in the others. Pressure pulse measurements as well as high-speed movies were made in all cases. Acoustic tracking methods were tested as well as thermocouple responses to bubble-gas temperatures. The cover-gas pressure was monitored, and samples were taken to discover if aerosol or fuel vapor had risen through the water. Some fuel transport was detected when the water temperature was 364 K but none at lower temperatures. A possible fuel-coolant interaction was noted in a test at 339 K, although no aerosol was detected in the cover gas. In three of the tests, thermocouples were installed at various levels directly above the test sample but little temperature change was detected, probably because of slow time response. On the other hand, results of pressure transducer measurements in the argon cover gas indicate that they may be useful in estimating bubble sizes in undersodium tests, and more evaluation of this technique is warranted.

In the CRI-III Facility, five of the tests were in a vacuum as part of the "Sandia Normalization Series" to compare CDV-produced fuel debris with that generated in Sandia's Annular Core Research Reactor (ACRR). The tests were conducted to test a new viewing system for temperature measurement. High-speed movies show that the windows, although quite small, cause major changes in electrical discharge so that temperature estimation is unsatisfactory.

The remaining CRI-III tests were performed in argon gas environment and were aimed at improving various aspects of the CDV technique, as well as providing an opportunity for impactor sampling of agglomerating aerosol. In the last of these tests, 5 g of aerosol were made airborne.

Activities connected with NSPP secondary containment aerosol studies included analysis of data from uranium oxide Test 207 and mixed oxide Tests 306 and 307. Test 207 was an attempt to reach concentrations of the order of 20 $\mu g/cm^3$ using the plasma torch (PT) generator, but only 3.2 $\mu g/cm^3$ was achieved because of UO_2 accumulation in the torch outlet. Cascade impactor measurements of aerosol mass median diameter were made over the first 24 h.

In mixed oxide Test 306, a sodium oxide aerosol generated by a 26-min sodium fire was allowed to agglomerate for 18 min; a uranium oxide aerosol was then generated for 13 min by a PT. The peak concentration of sodium oxide was 20 $\mu g/cm^3$, while the highest measured uranium oxide concentration was 3.3 $\mu g/cm^3$. The data indicate that the two aerosols were coagglomerating. After 48 h 90.3% of the sodium oxide aerosol and 73.7% of the uranium oxide settled on the floor. Almost all of the remainder plated on internal surfaces, and negligible quantities were still suspended.

In Test 307, the uranium oxide aerosol was generated first and allowed to agglomerate for 20 min. A sodium pool fire was then started, lasting for 12 min. The uranium oxide peak concentration was 6.5 $\mu g/cm^3$. Again, this test indicated coagglomeration and the effectiveness of a newly generated agglomerating aerosol in removing an existing aerosol. As in Test 306, cascade impactor measurements of particle diameter were performed.

Basic aerosol studies in the CRI-II Facility include mixed oxide aerosol generation by using PT generation for the uranium combined with a sodium spray burn. About 100 g of each aerosol is generated in this way. Spiral centrifuge, cascade impactor, and filter sample data for uranium-sodium ratios are compared as functions of time. In all transmission electron microscope (TEM) photographs, sodium clusters appear always to be associated with U_3O_8 chains with no evidence for unattached sodium.

In the analytical program, a simplified method for calculating bubble-liquid interface temperatures for analysis of FAST experiments is discussed as an alternative to finite-difference or numerical integration techniques. A simple formula believed to be of satisfactory accuracy is presented.

GLOSSARY OF ACRONYMS

ACRR	A nular Core Research Reactor
AMMD	aerodynamic mass median diameter
ART	Aerosol Release and Transport
CDV	capacitor discharge vaporization
CRI	Containment Research Installation
FAST	Fuel Aerosol Simulant Test
GSD	Geometric Standard Deviation
HCDA	hypothetical core-disruptive accident
LASL	Los Alamos Scientific Laboratory
LMFBR	Liquid-Metal Fast Breeder Reactor
NRC	Nuclear Regulatory Commission
NSPP	Nuclear Safety Pilot Plant
ORNL	Oak Ridge National Laboratory
PT	plasma torch
TEM	transmission electron microscope

LMFBR AEROSOL RELEASE AND TRANSPORT PROGRAM QUARTERLY PROGRESS REPORT FOR JANUARY–MARCH 1980

T. S. Kress M. L. Tobias

ABSTRACT

This report summarizes progress for the Aerosol Release and Transport Program sponsored by the Division of Reactor Safety Research of the Nuclear Regulatory Commission for the period January–March 1980. Topics discussed include (1) recent capacitor discharge vaporization (CDV) experiments conducted underwater in the Fuel Aerosol Simulant Test Facility to evaluate the disassembly process, including bubble dynamics and UO_2 vapor condensation and transport; (2) tests in the CRI-III vessel to evaluate UO_2 temperatures during melting and CDV discharge; (3) analysis of data from a uranium oxide experiment and two mixed oxide experiments in the Nuclear Safety Pilot Plant; (4) basic aerosol experiments on mixed oxide aerosols generated in the CRI-II Facility; and (5) presentation of a simplified method for calculating bubble-liquid interface temperatures for FAST experiment analysis.

Keywords: aerosol, core meltdown, hypothetical accident, LMFBR fission product release, fission product transport, ex-reactor experiment, safety, radionuclide transfer.

---

1. INTRODUCTION

The Aerosol Release and Transport (ART) Program at Oak Ridge National Laboratory (ORNL), sponsored by the Division of Reactor Safety Research of the Nuclear Regulatory Commission (NRC), is a safety program concerned with radionuclide release and transport. Its scope includes radionuclide release from fuel, transport to and release from primary containment boundaries, and behavior within containments. The overall goal of the program is to provide the analytical methods and experimental data necessary to assess the quantity and transient behavior of radionuclides released from reactor cores as a result of postulated events of varying severity up to and including accidents resulting in core melting.

The program is divided into several related experimental and analytical activities:

1. development of a capacitor discharge vaporization (CDV) system for deposition of energy in simulated fuel (UO_2) that will provide a nonnuclear means for studying fuel response to energy depositions characteristic of severe accident conditions;

2. study of fuel interactions, expansion, and thermal behavior within the sodium pool as the resultant fuel-vapor bubble is produced and transported through the sodium to the cover-gas region;
3. development of alternative means for generating fuel-simulant aerosols on a relatively continuous basis;
4. study of the characteristics and behavior of fuel-simulant aerosols in several small vessels; and
5. production and study of fuel-simulant and sodium aerosols in the Nuclear Safety Pilot Plant (NSPP) for the validation of models, with particular emphasis on the behavior of mixtures of the two nuclear aerosol species.

Varying levels of effort are anticipated within these categories, with analytical models accompanying the experimental work. Analytical requirements fall into three categories: (1) fuel response to high rates of energy deposition, (2) fuel-bubble dynamic behavior and transport characteristics under sodium, and (3) dynamic aerosol behavior at high concentrations in the bubble and containment atmospheres.

An attempt will be made to consolidate the analyses and data and to present them in a manner that will facilitate direct assessment of the radiological hazard associated with arbitrary hypothetical accident scenarios.

2. EXPERIMENTAL PROGRAM

2.1 Source Term and SIMMER Verification Experiments in FAST/CRI-III

A. L. Wright A. W. Smith
J. M. Pochelle

2.1.1 Introduction

The Fuel Aerosol Simulant Tests (FAST) and the Containment Research Installation-III (CRI-III) tests are performed by using the CDV technique to place uranium dioxide fuel samples into the high-energy states that could be produced in severe reactor accidents. The primary goals of the FAST/CRI-III test program are to (1) use the experimental results as a base for developing analytical models that could then be used to predict fuel transport through the coolant in case of an accident and (2) perform experiments in support of the program to verify models in the Los Alamos Scientific Laboratory (LASL) SIMMER computer code.

During this quarter, 18 tests were performed in the FAST/CRI-III Facility, including 8 underwater tests in the FAST Facility and 10 tests in the CRI-III facility. Test specimen and electrical energy input data are presented in Tables 1 and 2. Individual test results and conclusions are presented in Sects. 2.1.2 and 2.1.3.

2.1.2 Discussion of results from FAST underwater tests

Eight underwater tests were performed in the FAST Facility this quarter. A number of these were performed at conditions outlined in the FAST experimental plan.[1] For all of these tests, the argon cover-gas pressure was slightly greater than 0.101 MPa. Parameters varied in the tests were the pressure of xenon gas trapped in the test sample, the water temperature, and the water height above the test sample. A summary of the pressure, temperature, and liquid height settings is presented in Table 3.

During many of the tests, measurements were made of the pressure pulses produced by bubble expansion and contraction. A Kaman Sciences pressure transducer was mounted ~229 mm from the test sample; pressure signals were recorded for >80 ms after capacitor discharge. High-speed movies were taken of all tests. In addition to movies, other techniques were used to try to "track" the bubbles formed: acoustic measurements, measurements of pressure changes in the argon cover gas, and attempts to use thermocouple response to the bubble-gas temperatures to detect bubbles. Finally, a few minutes after capacitor discharge, the argon gas above the water was sampled to determine if any fuel vapor or aerosol had been transported through the water during the tests.

FAST 42. The setup for this test was the same as for FAST 40; an acoustic transducer was mounted on the vessel at the level of the test sample. The "time-of-flight" for an acoustic pulse to be transmitted, reflected from the bubble interface, and received by the sender transducer was recorded as a function of time for both tests and is shown in Fig. 1.

Table 1. Sample data

Test	Pellet stack		Microsphere mass (g)	Quartz tube dimensions (mm)	
	Mass (g)	Length (mm)		ID	OD
FAST 42	17.63	91.7	31.31	9.70	16.78
FAST 43	17.60	91.9	32.42	9.73	16.87
FAST 44	17.43	90.7	32.34	9.70	16.63
FAST 45	17.58	90.3	32.62	9.70	17.28
FAST 46	17.27	89.7	32.55	9.72	16.90
FAST 47	17.58	90.3	32.36	9.70	17.48
FAST 48	17.25	89.7	32.77	9.70	17.23
FAST 49	17.43	89.7	32.76	9.72	17.18
CDV 91	21.58	112.4	37.42	9.70	16.51
CDV 92	21.23	110.6	38.91	9.71	16.24
CDV 93	21.47	110.6	39.04	9.72	17.06
CDV 94	21.56	112.1	39.19	9.72	16.86
CDV 95	21.73	112.0	40.57	9.73	16.74
CDV 96	17.58	90.5	32.82	9.70	17.28
CDV 97	21.24	110.3	39.88	9.70	16.98
CDV 98	17.61	91.4	31.78	9.70	17.35
CDV 99	17.34	90.1	30.81	9.70	17.49
CDV 100	17.04	88.5	31.90	9.75	17.49

Table 2. Preheat and capacitor discharge data[a]

Test	High-preheat power (W)	Sample resistance after high preheat (Ω)	CDV time to arcing (ms)	CDV energy input to arcing (kJ)
FAST 42	1700	0.43	1.83	21.4
FAST 43	1700	0.49	2.95	32.1
FAST 44	1700	0.45	3.55	41.1
FAST 45	1700	0.46	3.23	35.9
FAST 46	1700	0.46	3.67	41.4
FAST 47	1700	0.44	2.58	29.9
FAST 48	1700	0.46	3.69	32.6
FAST 49	1700	0.43	2.32	26.2
CDV 91	2200	0.45	2.30	25.1
CDV 92	2200	0.49	2.56	27.3
CDV 93	2200	0.49	0.45	3.6
CDV 94	2200	0.47	2.26	21.2
CDV 95	2200	0.47	2.13	22.0
CDV 96	1700	0.49	3.43	38.3
CDV 97	2200	0.49	No capacitor discharge	
CDV 98	1700	0.46	No capacitor discharge	
CDV 99	900	1.67	8.78	51.6
CDV 100	1400	0.59	5.24	43.5

[a]Five capacitor banks were charged to ~1750 V (75 kJ) in FAST 48, CDV 99, and CDV 100. No capacitor discharge was performed in CDV 97 and 98. In other tests, four banks were charged to ~1950 V (~75 kJ).

Table 3. Pressure, temperature, and liquid height conditions for FAST underwater tests 42 through 49

Test	Gas pressure (MPa)		Water	
	Argon[a]	Xenon[b]	Temperature (K)	Height[c] (mm)
FAST 42	0.108	0.513	298	1120
FAST 43	0.111	0.513	364	1120
FAST 44	0.122	0.513	339	1120
FAST 45	0.123	0.513	298	1120
FAST 46	0.122	0.513	363	1120
FAST 47	0.122	0.513	298	710
FAST 48	0.122	~0	298	1120
FAST 49	0.122	0.513	298	710

[a]This refers to the argon gas space above the water.

[b]Xenon gas is inserted into the fuel test sample; after capacitor discharge, xenon becomes part of the bubble produced.

[c]This refers to the water height above the level of the test sample.

As can be seen, the data look different for the two tests. Time-of-flight data for FAST 42 would seem to indicate that the bubble collapse took longer than in FAST 40. Actually, the first bubble collapse in FAST 42 occurred ~50 ms after sample burst, while in FAST 40 the first collapse occurred more than 80 ms after sample breakup. However, in both tests the transducer seal to the vessel broke at some time after capacitor discharge; it may be that real time-of-flight information was not obtained in either test.

FAST 43. This was the third high-temperature water test that we have performed. Pressure measurements indicated that the time between the initial formation of the bubble and the first collapse and reexpansion of it was ~90 ms. This is 40 ms longer than in tests where the water was not heated and where the argon and xenon gas pressures were at the levels used in FAST 43. This indicates that a significant amount of water vaporization — producing a larger bubble — occurs in high-temperature water tests.

Also, as in the other hot-water tests, aerosol measurements in the cover gas indicated that a few milligrams of fuel were transported through the water to the cover gas.

FAST 44. Water temperature for this test was 339 K, an intermediate level among the temperatures used in previous tests. CDV energy input was high for this test, and the steel tube totally broke away from the sample.

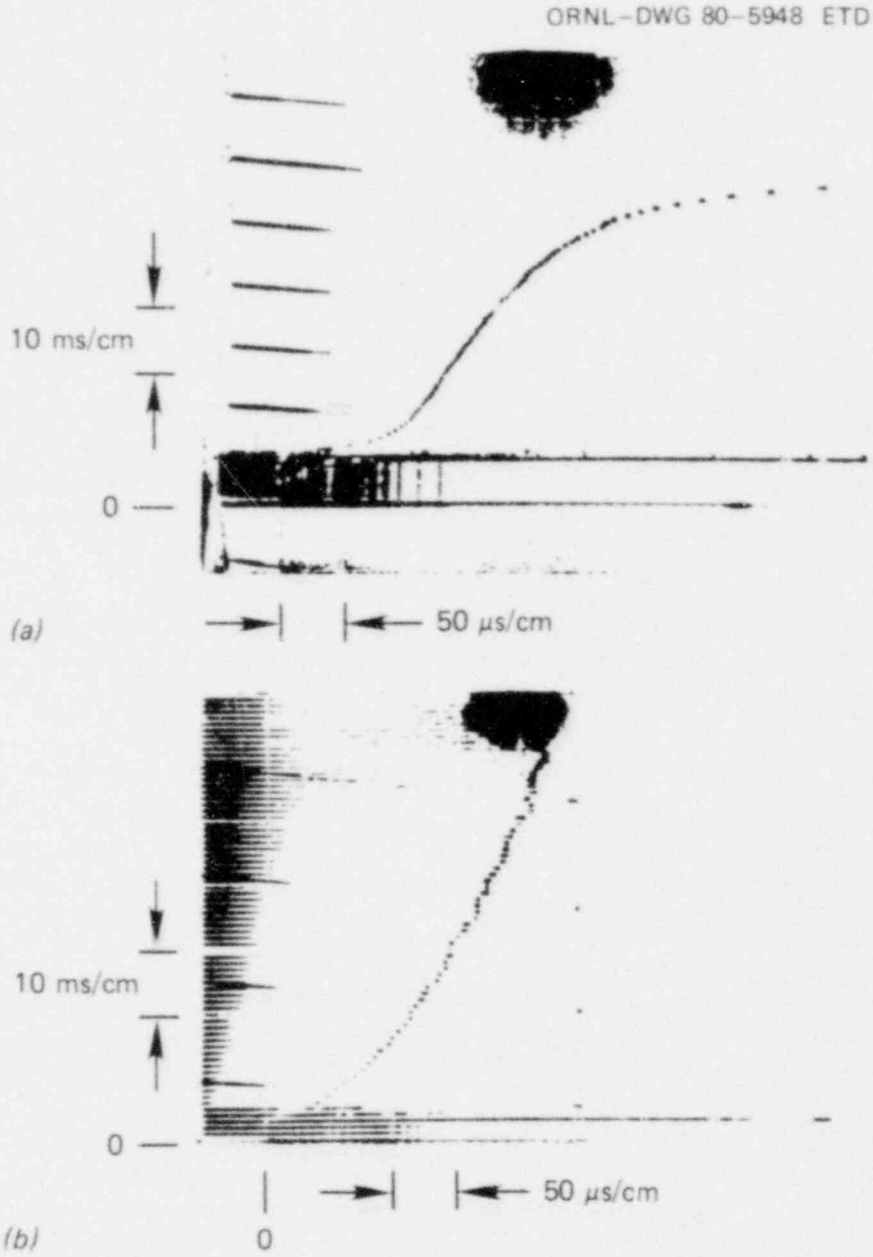

Fig. 1. "Time-of-flight" data from acoustic bubble detection measurements made in (*a*) FAST 40; (*b*) FAST 42. Time-of-flight data on horizontal axis; experiment time (from start of CDV) on vertical axis.

The measured pressure due to bubble expansion and collapse is shown in Fig. 2. The measured peak burst pressure was somewhat higher than that usually found; the most interesting result, however, is that the second pressure spike was larger than the first. This is a possible indication that a fuel-coolant interaction occurred during bubble collapse, perhaps because of efficient fuel-water mixing.

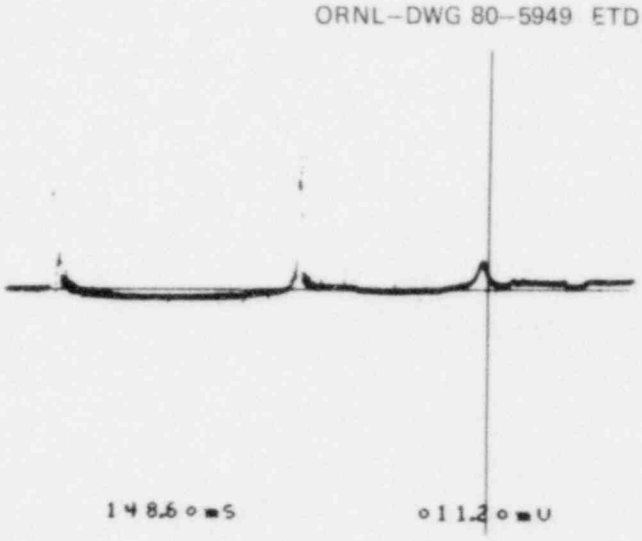

Fig. 2. Pressure data from FAST 44 (pressure measured underwater, 229 mm from test sample). Note that second pressure pulse, which occurred ~80 ms after sample burst, is larger in magnitude than burst pulse.

No aerosol was found in the cover gas after this test. Comparison with the resulting aerosol transport found in FAST 43 may indicate that the lowered water temperature in FAST 44 led to less water vaporization and/or more rapid condensation of the water-vapor bubbles (perhaps containing fuel aerosol) that were formed.

FAST 45. In this test an array of thermocouples was put into the water, with thermocouples placed at various levels directly above the test sample. Also, as in FAST 42, measurements were made using an acoustic transducer coupled to the vessel wall. The pressure transducer in the water was removed for this test (and for FASTs 46 and 47), and the 5000-W lamp was beamed through this port to improve the illumination of the fuel bubble for the high-speed movies. Finally, pressure measurements were made in the argon cover-gas region, using a Kaman Sciences pressure transducer (3.44 MPa maximum pressure rating).

CDV energy input was large, and a loud shock was produced. Surprisingly, there was no observed temperature response from the thermocouples, even from the four that were ~100 mm from the test sample. This probably indicates that their inherent time response — >100 ms — is simply too long to permit response to the rapidly oscillating bubble produced. The response (time-of-flight data) measured using the acoustic transducer looked like that from FAST 40 [Fig. 1(a)], and again the transducer broke away from the vessel sometime after capacitor discharge.

Data from the pressure transducer in the argon cover gas (Fig. 3), are quite interesting. The maximum in the cover-gas pressure should be occurring roughly when the maximum bubble volume occurs. Assuming an isentropic compression of the cover gas from its initial pressure to the maximum measured value, the maximum estimated bubble diameter is ~210 mm, or about 8.3 in., which is not unreasonable. Pressure measurements in the

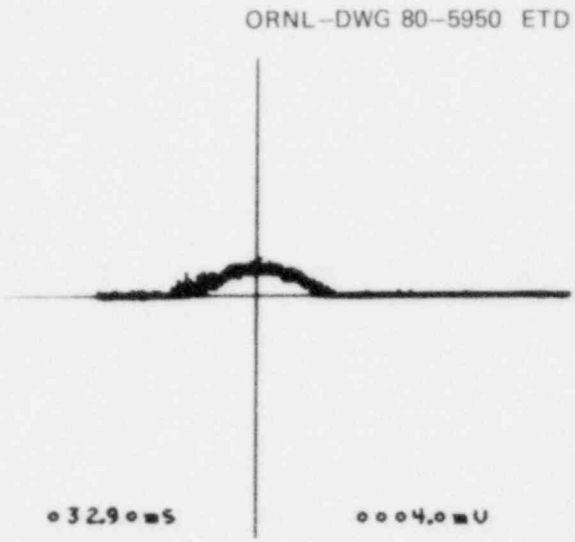

Fig. 3. Pressure transient measured in argon cover gas in FAST 45. Peak pressure occurred ~32.9 ms after start of capacitor discharge.

cover gas may prove useful in estimating bubble sizes produced in under-sodium tests; more tests will be done to evaluate the usefulness of these measurements.

The high-speed movie results were quite interesting because they indicated that many water vapor bubbles were produced sometime after the first few bubble oscillations. These bubbles and some xenon gas that remained in the steel housing that holds the sample spring-loading system and current-carrying electrode rose through the viewport area after fuel-bubble oscillations ceased. The small water-vapor bubbles were probably formed by contact of water with liquid/solid fuel that remained in the vessel after fuel vaporization.

FAST 46. The thermocouple array and argon-gas region pressure transducer were installed in this high-temperature water test. Output from the pressure transducer is shown in Fig. 4. The estimated maximum bubble diameter for this test was ~210 mm, or 8.3 in. Note that this diameter is larger than that estimated for FAST 45, as expected, because significant water vaporization into the bubble should have occurred. Also note that, even though there seemed to be a shift in the pressure baseline, a second pressure increase (which would correspond to bubble reexpansion) occurred.

There was a slight temperature rise (4 to 5 K) in the temperatures measured by the thermocouples that were ~100 mm from the sample; however, because of the long thermocouple response time, this temperature rise was meaningless in terms of bubble detection.

The high-speed movies again showed that a large number of water-vapor bubbles rose through the water after the main bubble disappeared. Such bubble formation should not occur in sodium tests because of sodium's excellent heat transfer characteristics.

Of the four high-temperature water tests, this was the only one where no aerosol was found in the cover gas.

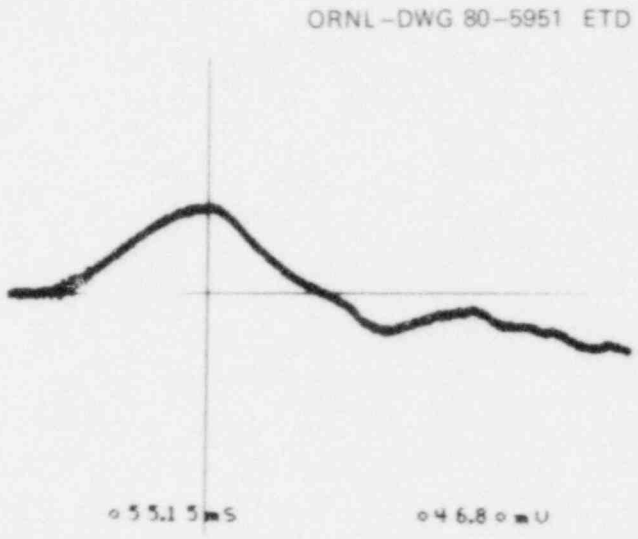

Fig. 4. Pressure transient measured in argon cover gas in FAST 46. Peak pressure occurred ~55.15 ms after start of capacitor discharge.

FAST 47. This was the first water test where the water level was reduced to 710 mm. Pressure measurements in the argon were attempted, but a transducer zero shift at the start of capacitor discharge made these measurements meaningless. The thermocouple array was again installed, and a 4 to 5 K temperature increase was measured by the thermocouples near the sample. No aerosol was found in the cover gas after the test.

FAST 48. This test was done with essentially no xenon gas in the sample, similar to conditions for CDV 90 performed last quarter.[2] In CDV 90, movies indicated that the bubble seemed more persistent than in tests where xenon is present in the bubble. For this test an acoustic transducer was coupled to the vessel in such a way that the transducer would not lose contact during the experiment.

The CDV energy input was above 30 kJ, but steel tube rupture was very poor. Time-of-flight data from the acoustic measurements are shown in Fig. 5; the transducer did not fall off the vessel in this test. The noisy nature of the data is possibly due to the poor steel tube rupture and resulting nonuniform bubble formation.

Fuel aerosol was not transported to the cover gas in this test.

FAST 49. This was the second test performed with low water height. In the test, steel tube rupture was poor and no useful data were obtained from the pressure transducers.

2.1.3 Discussion of results from CRI-III tests

Ten experiments were performed in the CRI-III Facility this quarter. The first five of these (CDVs 91 through 95) were performed in a vacuum and were related to follow-on tests in the "Sandia Normalization" test series.[3,4] The remaining tests were related to achieving a better understanding of the CDV process and improvement of the technique.

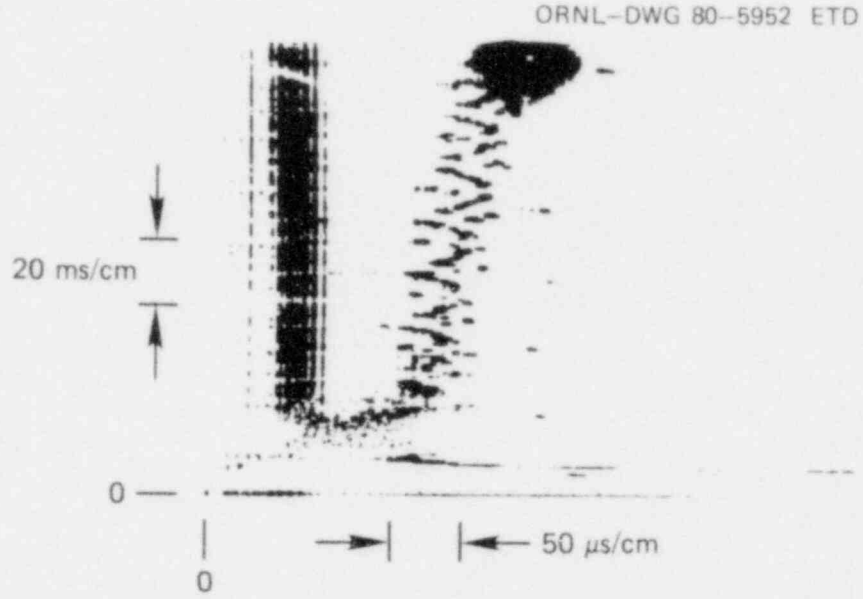

Fig. 5. "Time-of-flight" data from acoustic bubble detection measurements made in FAST 48. Time-of-flight data on horizontal axis; experiment time (from start of CDV) on vertical axis.

CDV 91. The purpose of the Sandia Normalization tests is to compare the fuel debris produced — at comparable sample energy levels — by electrical (CDV) energy input to that produced by neutronic energy input in Sandia's Annular Core Research Reactor (ACRR). Such a comparison requires measurement of fuel pellet temperatures after capacitor discharge. The viewing setup in the previous tests[4] used a quartz tube that had a "necked-down" section such that all of the microspheres were pushed away from a portion of the pellet. Temperature measurements were made of the exposed pellet using a photographic method. However, this viewing system seemed to result in a large perturbation in the current flow through the sample, and temperature measurements were unreliable.

The viewing system proposed for follow-on Sandia tests is shown in Fig. 6. In this setup, a small view window exposes only a portion of the pellet. A 0.39-mm-diam hole was bored to the pellet center; both the pellet surface and center temperatures, in principle, can be measured. CDVs 91 through 95 were an attempt to determine the feasibility of this fuel viewing setup.

The view window used in CDV 91 was 4.8 mm wide and 6.4 mm long (along the pellet stack length). One camera was run at 200 frames/s to film preheat, while the other camera, set at 10,000 frames/s to film capacitor discharge, did not run. The CDV energy input was roughly that achieved in the previous Sandia vacuum tests. Although the slow-speed camera ran, it was not focused on the view window so no useful information on preheat was obtained.

CDV 92. This test was done with a smaller window (2.4 mm wide) than that used in CDV 91. Both cameras ran for this test. The preheat film indicated that the exposed pellet cracked along its length in the vicinity

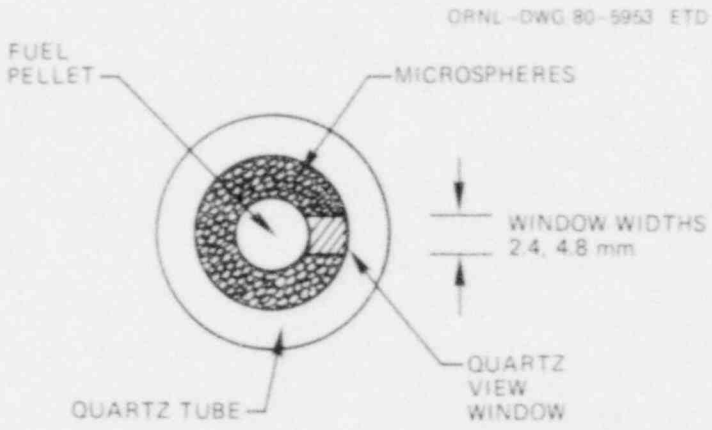

Fig. 6. Drawing of CDV sample cross section illustrating "view window" installed in CDVs 91 through 95.

of the hole, and molten fuel could be seen through the crack and in the hole during high preheat. Near the end of preheat there was a microsphere region around the window where the microspheres looked colder than those further from the window. The capacitor discharge film indicated that the fuel in the window region was heating up less rapidly than that fuel which was totally surrounded by microspheres. These results indicate that current shunting was occurring because of the presence of the quartz window in the sample.

CDV 93. The larger view window, like that used in CDV 91, was installed. Capacitor discharge was very short, and no useful information was obtained from the filming. The preheat film was very similar to that from CDV 92.

CDV 94. This test again used the larger window of the type installed in CDVs 91 and 93. The capacitor discharge phase was unusual, with a small arc produced at ~1 ms, followed by sample rupture and arcing at 2.26 ms. Movie results for preheat and capacitor discharge again resembled those from CDV 92.

CDV 95. The view window used was smaller than in the previous four tests (2.4 mm wide and 3.2 mm long). Hopefully, this change would reduce the perturbation in fuel heating due to the presence of the window. However, the visual results from the preheat and capacitor discharge movies were much like those for CDVs 92 and 94.

Results from the test movies indicate that even the small view windows cause a major change in the electrical discharge through the fuel in the vicinity of the windows. During the next quarter, we will attempt to put layers of microspheres between the exposed pellet and the view window. The number of microsphere layers can be varied, and the temperature data obtained for various layers hopefully can be extrapolated to the condition where no window is present.

CDV 96. This argon test was done (a) with the aim of producing a high-energy input and high-aerosol yield and (b) impactor samples of the

agglomerated aerosol to be taken at various times after capacitor discharge.* As hoped, a high-CDV energy input was achieved and indications from mass sampler data were that 4 to 5 g of aerosol was made airborne. Impactor sampling results will be discussed in the CRI-II program portion of this report (Sect. 2.3).

CDV 97. This was a "preheat-only" test, using the 16-pellet stack (~110-mm length), and 2200-W high preheat. The sample was to be sectioned after the test, and the cross sections were to be polished and photographed to determine pellet melt fractions for this preheat level. Results will be reported next quarter.

CDV 98. This was another "preheat-only" test, using the 13-pellet stack (~90-mm length), and 1700-W high preheat. As in CDV 97, photographic results of sample sectioning will be reported next quarter.

CDV 99. This was an attempt to duplicate the results of CDV 85, a "heat-through-melt" test[5] where a 900-W high preheat was used. All test conditions were the same as in CDV 85. However, sample resistance after high preheat was 1.66 Ω, considerably less than the 2.1-Ω value from CDV 85. Consequently, as shown in Fig. 7, the time where the abrupt current decrease occurred during capacitor discharge — attributed to fuel melting and a decrease in the UO_2 electrical conductivity through melt — is ~1 ms less in CDV 99 than in CDV 85. Another difference between the two tests is that in CDV 99 the observed current decrease was not as steep or as great as in CDV 85. Capacitor discharge occurred for 8.78 ms, and about 4 g of aerosol was produced.

---

*All impactor sampling in these experiments was performed by George Parker.

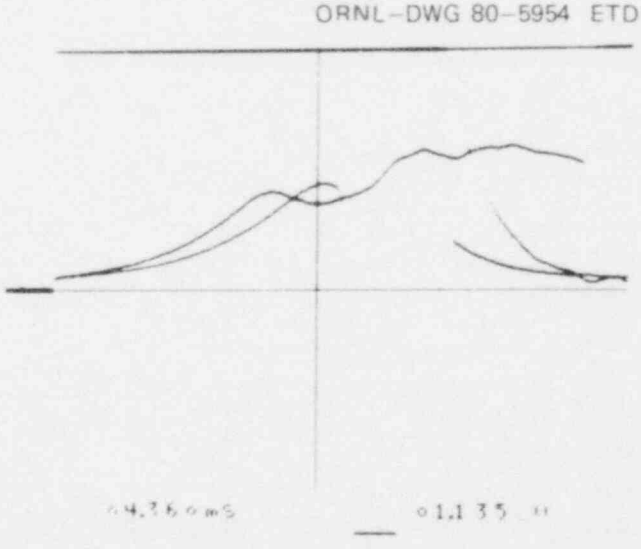

Fig. 7. CDV current vs time data for CDVs 85 and 99. "Heat-through-melt" tests performed at 900-W high preheat. Current decrease (due to fuel melt) in CDV 99 occurred ~1 ms earlier than in CDV 85.

CDV 100. This was a "heat-through-melt" test (during capacitor discharge) where the high-preheat level (1400 W) was near the 1700-W level usually used when pellet melting during preheat is desired. At 1.99 ms after the start of capacitor discharge, an ~20% decrease in current was observed. This test is consistent with tests like CDV 83, where the high preheat was less (1200 W) and the current drop occurred at a later time (2.9 ms).

At least 5 g of aerosol was made airborne in this test. Impactor samples of the agglomerated aerosol were again taken.

2.2 Secondary Containment Aerosol Studies in the NSPP

R. E. Adams

2.2.1 Introduction

Activities of the NSPP during the period included analysis of data from a uranium oxide aerosol test (207) and performance of and analysis of data from two mixed oxide aerosol tests (306 and 307).

2.2.2 Uranium oxide aerosol Test 207

The purpose of this fourth test utilizing the PT aerosol generator was to produce an aerosol concentration approaching 20 $\mu g/cm^3$ so that the results could be compared with those from the mixed oxide aerosol tests where the total mass concentration was in this range. This test differed from previous uranium oxide aerosol tests in that aerosol samples were to be taken during the generation period to define the early increase in aerosol concentration. The desired concentration level was not achieved because of a larger-than-anticipated accumulation of uranium oxide in the generator outlet.

Aerosol mass concentration. The aerosol was generated over a 26-min period, and four aerosol samples were taken during this period. The maximum measured aerosol concentration was 3.2 $\mu g/cm^3$ at 23 min after start of aerosol generation. Aerosol mass concentrations as a function of time are given in Fig. 8.

Aerosol particle size. The aerodynamic mass median diameter (AMMD) of the aerosol was measured with cascade impactors (Andersen Mark III) over the first 24 h of the test. The results are listed in Table 4. Sample 7 contained a sufficient quantity of uranium oxide for analysis; however, the distribution deviated significantly from log normal, and t e mass median diameter could not be determined.

Aerosol distribution. At the termination of the test (48 h), the approximate aerosol distribution, as determined by the fallout and plateout samplers and the final filter samples, was as follows: aerosol settled on floor of the vessel, 78%; aerosol plated on internal surfaces, 22%; aerosol still suspended in the vessel atmosphere, <0.02%.

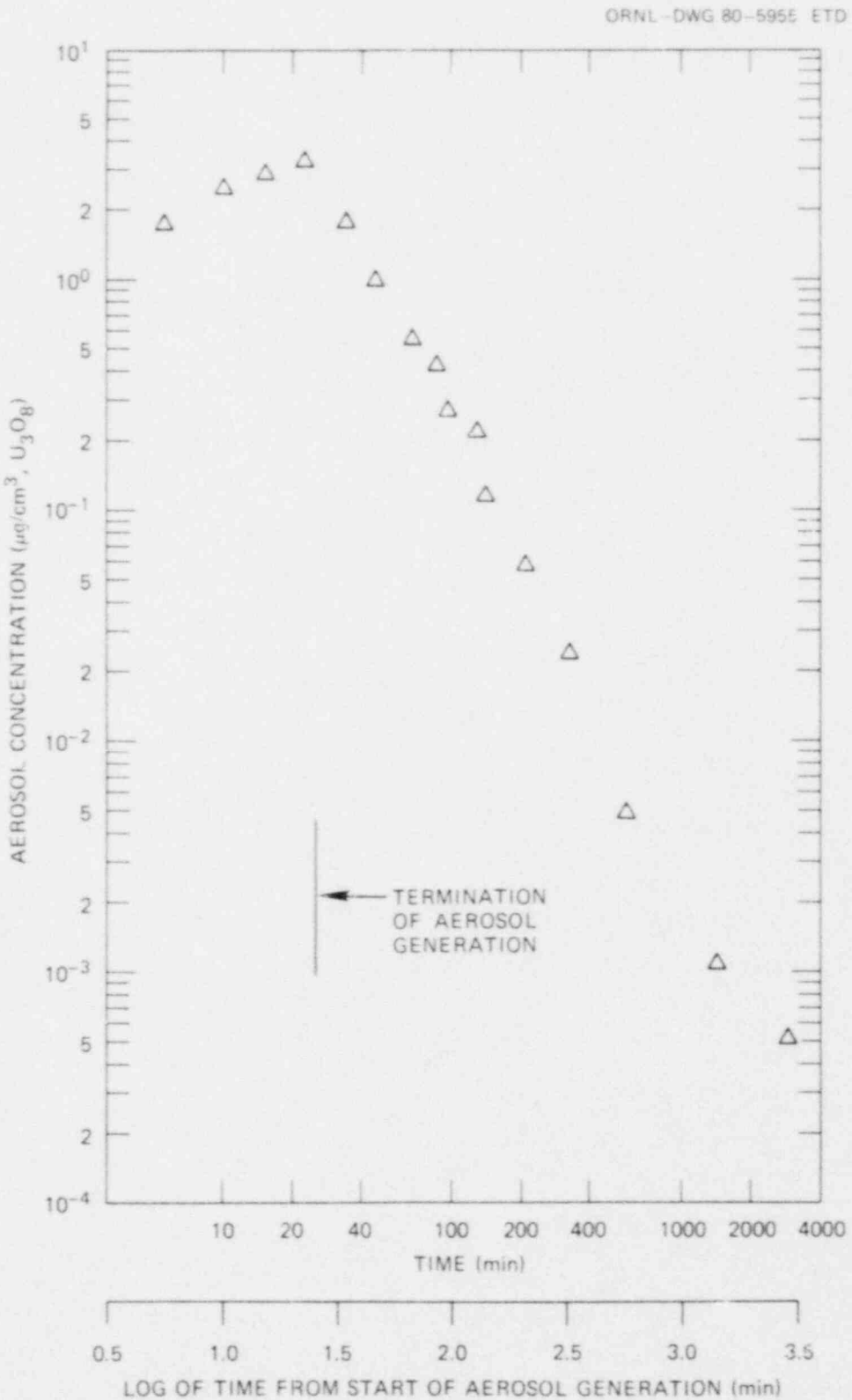

Fig. 8. Average uranium oxide aerosol concentration — Test 207.

Table 4. Uranium oxide aerosol particle size — Test 207

Sample No.	Time (min)	AMMD[a] (μm)	σ_g[b]
1	25.2	2.5	3.8
2	61.5	2.6	2.5
3	108.4	2.9	2.9
4	222.5	2.8	2.4
5	346	1.9	2.8
6	594	1.3	2.5
7	1467	(See text)	

[a]Aerodynamic mass median diameter.

[b]Geometric standard deviation.

2.2.3 Mixed uranium oxide–sodium oxide aerosol Test 306

The purpose of this test was to mix an aged (agglomerated) sodium oxide aerosol with a newly generated uranium oxide aerosol and investigate the influence of aerosol particle size on the agglomeration process. The sodium oxide aerosol was produced by a sodium pool fire of 26 min duration and was then allowed to agglomerate for an additional period of 18 min. Uranium oxide aerosol generation (by the PT generator) was then initiated and continued for 13 min. The vessel atmosphere was air at a relative humidity of <20%, and the initial pressure and temperature were slightly above ambient because of preheating of the sodium burn pan and internal sodium delivery lines. Test duration was 48 h.

Aerosol mass concentration. A peak sodium oxide aerosol concentration of 20 $\mu g/cm^3$ was measured, and the concentration had dropped to about 4 $\mu g/cm^3$ when the uranium oxide aerosol generation was initiated. Upon introduction of the uranium oxide, the concentration of the sodium oxide aerosol decreased significantly. Aerosol samples taken 3 min after the end of the uranium oxide aerosol generation period indicated concentrations of 0.36 $\mu g/cm^3$ for sodium oxide and 3.3 $\mu g/cm^3$ for uranium oxide. The sodium oxide aerosol concentration was reduced by about 92% over the 16-min period between start of uranium oxide aerosol generation and the extraction of the first mixed oxide aerosol sample. This behavior, supported by the fallout data, suggested that the two aerosols were coagglomerating. Figure 9 contains data on aerosol mass concentration as a function of time and also shows results from comparable single-component tests with either sodium oxide or uranium oxide aerosols.

Aerosol particle size. Cascade impactor measurements for aerodynamic aerosol particle size were made over the first 9.7 h of the test. Results are listed in Table 5. The aerosol material collected on each plate of

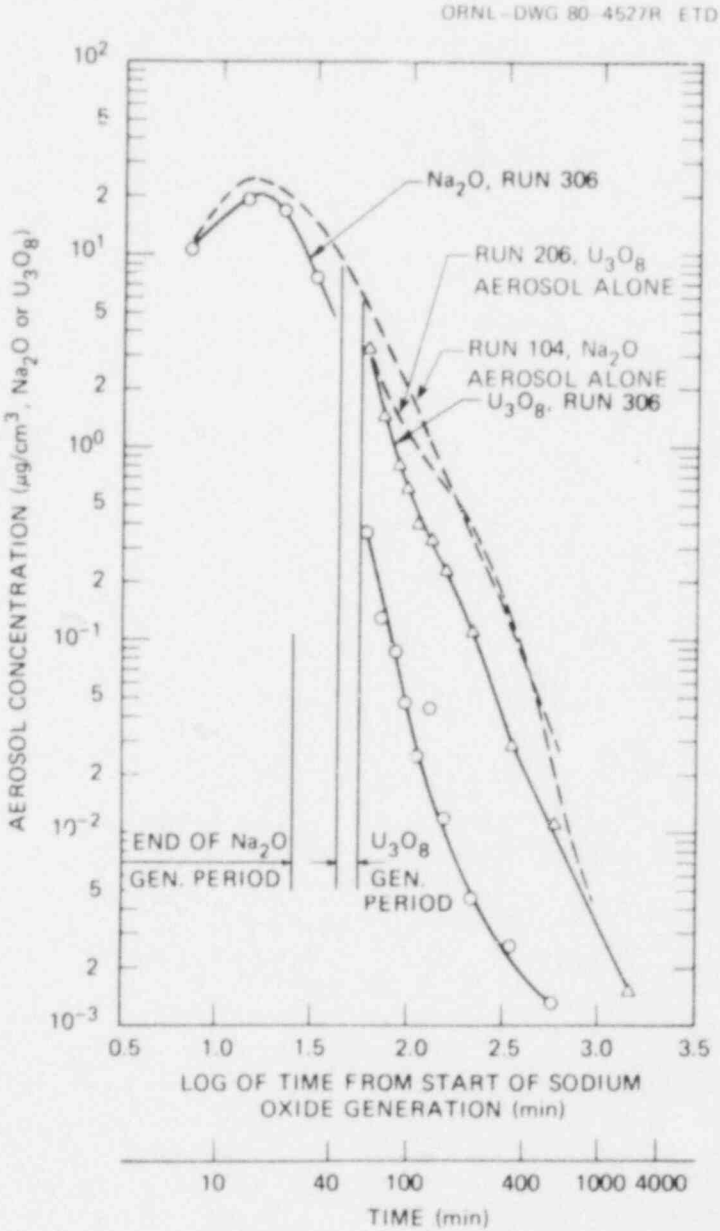

Fig. 9. Average concentrations of individual components of mixed oxide aerosol Test 306 and comparable single-component aerosol tests.

the impactor was analyzed for both sodium and uranium content. Normally, an aerodynamic mass median particle diameter is determined on the basis of the uranium oxide content or the sodium oxide content or the total mass. If the particle diameters calculated using these three values were similar, this would have been further evidence of the coagglomeration process. However, for this test, the sodium oxide content of the mixed oxide aerosol was too low and was not adequate for a particle size determination. These values were used, however, in calculating the particle diameter using the total aerosol mass.

Table 5. Mixed uranium-sodium oxide aerosol particle size — Test 306

Sample No.	Time (min)	AMMD[a] calculated by using the					
		Uranium oxide component		Sodium oxide component		Total aerosol mass	
		AMMD (μm)	σ_g[b]	AMMD (μm)	σ_g	AMMD (μm)	σ_g
1	35.5	(No uranium)		3.9	2.2		
2	63.4	2.6	2.1			3.0	2.4
3	89	3.0	2.7			3.4	2.9
4	139	3.1	2.8			3.0	3.0
5	236	2.4	2.3			2.3	2.5
6	344	1.9	2.5			1.9	2.5
7	581	(See text)					

[a]Aerodynamic mass median diameter.

[b]Geometric standard deviation.

Distribution of aerosol. At the termination of the test, the approximate distribution of the aerosol, as determined by the fallout and plateout samplers and the final filter samples, was as follows: aerosol settled on floor of the vessel, 90.3% (sodium oxide) and 73.7% (uranium oxide); aerosol plated on internal surfaces, 9.7% (sodium oxide) and 26.3% (uranium oxide); aerosol still suspended in the vessel atmosphere, 0.0009% (sodium oxide) and 0.006% (uranium oxide).

2.2.4 Mixed uranium oxide–sodium oxide aerosol Test 307

The purpose of this test was to mix an aged (agglomerated) uranium oxide aerosol with a newly generated sodium oxide aerosol and investigate the influence of particle size on the coagglomeration process. In effect, this test was the reverse of Test 306. The uranium oxide aerosol was generated for a period of 25 min and then allowed to agglomerate for a period of 20 min. Generation of the sodium oxide (by a pool fire) was then initiated and was continued for about 12 min. Vessel atmosphere conditions were essentially the same as for Test 306.

Aerosol mass concentration. A peak uranium oxide aerosol concentration of 6.5 $\mu g/cm^3$ was measured, and the concentration had decayed to about 1.6 $\mu g/cm^3$ when the sodium oxide aerosol generation was initiated. Upon introduction of the sodium oxide, the concentration of the uranium oxide aerosol decreased significantly. Aerosol samples taken at 5.7 min after the end of the sodium oxide aerosol generation period indicated concentrations of 0.12 $\mu g/cm^3$ for uranium oxide and 5.3 $\mu g/cm^3$ for sodium oxide. The uranium oxide aerosol concentration was reduced by about 92.5% over the 18-min interval between start of sodium oxide aerosol generation and the extraction of the first aerosol sample. This behavior supports

the observations made during Test 306 and further confirms that the two aerosols are coagglomerating. A newly generated, agglomerating aerosol is effective in removing an existing aerosol from an enclosed volume. Figure 10 illustrates the aerodynamic behavior of each component of the mixed oxide aerosol as a function of time.

Aerosol particle size. Cascade impactor measurements were made over the first 9.7 h of the test. Results are listed in Table 6. An AMMD was calculated for each component of the aerosol (where possible), as well as for the total mass. Data from sample 2 for uranium oxide was not usable; sample 7 contained only a small amount of material, and the size distribution deviated significantly from log normal.

Table 6. Mixed uranium-sodium oxide aerosol particle size — Test 307

Sample No.	Time (min)	AMMD calculated by using the: Uranium oxide component		Sodium oxide component		Total aerosol mass	
		AMMD (μm)	σ_g[b]	AMMD (μm)	σ_g	AMMD (μm)	σ_g
1	27.8	2.4	2.3	(None present)			
2	55	(Data not usable)		3.9	3.0	4.1	3.0
3	86.6	4.2	2.6	4.2	2.2	3.9	2.3
4	136.8	3.4	3.4	3.4	2.0	3.5	2.1
5	233	2.4	2.3	2.3	2.0	2.3	2.0
6	342	2.4	2.4	2.4	1.8	2.5	1.8
7	587	(See text)					

[a]Aerodynamic mass median diameter.

[b]Geometric standard deviation.

Distribution of aerosol. At the termination of the test, the approximate distribution of the aerosol, as determined by the fallout and plateout samplers and final filter samples, was as follows: aerosol settled on floor of the vessel, 82.7% (uranium oxide) and 75.3% (sodium oxide); aerosol plated on internal surfaces, 17.3% (uranium oxide) and 24.7% (sodium oxide); aerosol still suspended in the vessel atmosphere, essentially none.

2.3 Basic Aerosol Experiments in CRI-II

2.3.1 Introduction

The characterization of mixed oxide (U_3O_8·Na_2O_2) aerosols in the CRI-II Facility has been extended since the first results were reported in the July–September 1979 ART Quarterly Report.[5] In that report, the first

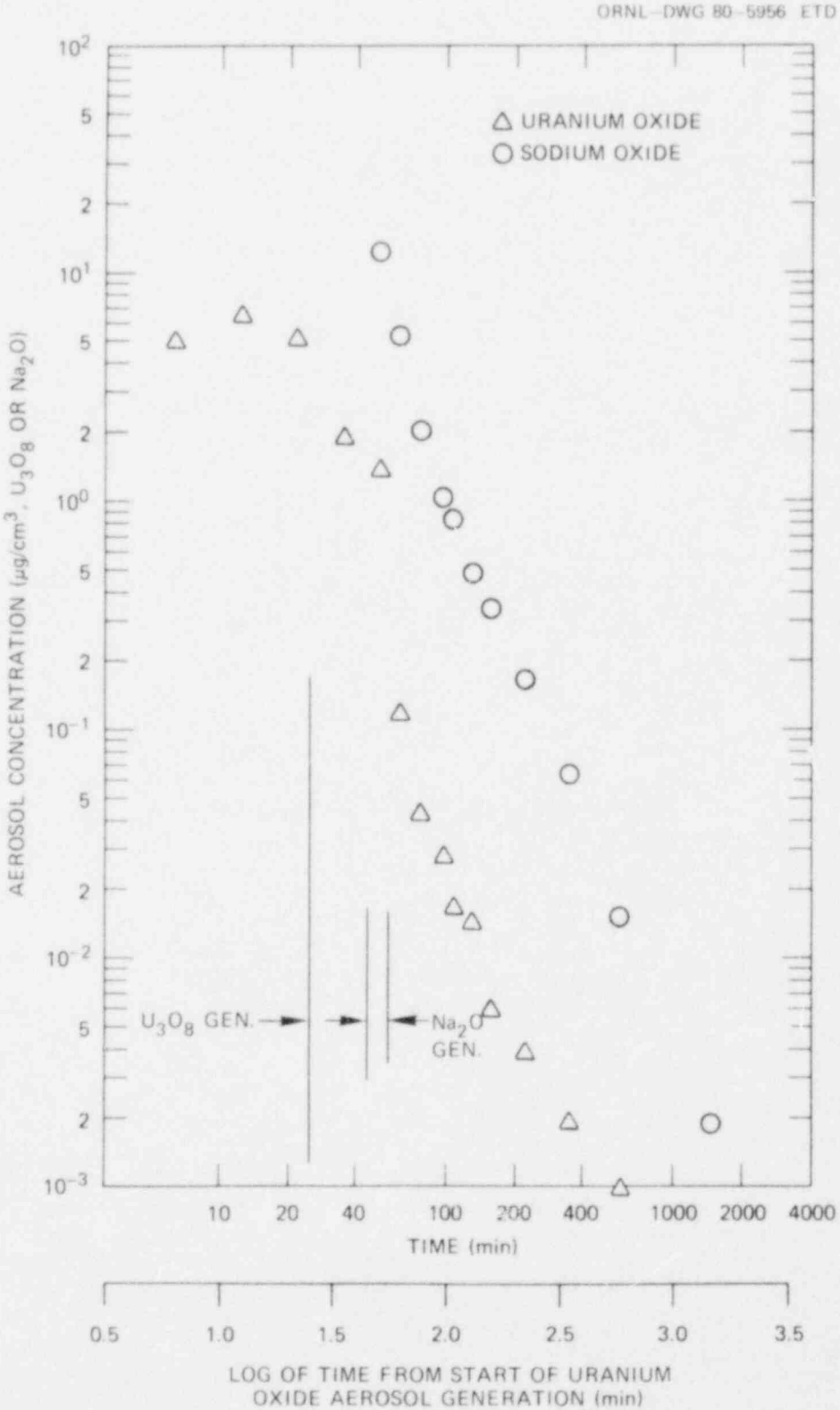

Fig. 10. Average concentrations of individual components of mixed oxide aerosol Test 307.

distinctly clear indications of the nature of the inclusion of sodium peroxide cluster aggregates in the U_3O_8 chains were shown in TEM photomicrographs enhanced by the use of a preservative organic coating on the sodium clusters. An interpretation of the mechanism of the inclusion, whether by coagglomeration or collision and interception cannot be clearly stated; however, additional insight is being obtained by more extensive photomicrography and by more accurate measurement of the ratios of the two components both in filter samples and in the various size distribution fractions obtained through cascade impactors and the spiral centrifuge.

2.3.2 Generation of mixed oxides in CRI-II

The current series of mixed oxide aerosols has been conducted in a nearly concurrent generation plan. This means that the metal-oxygen torch generator is initiated only slightly ahead (about 1 min) of the sodium spray, and the two operations are then allowed to proceed together for the duration of the time required to burn the sodium charge. This is usually about 1 min, and at that point the uranium burn is also terminated. About 100 g of airborne uranium oxide and somewhat less of sodium peroxide (because of lower dispersion efficiency of the sodium spray) are generated in this time interval. Obviously the uranium oxide primary particles are all preformed in very close proximity to the torch head, and to a somewhat less extent, the sodium oxide primary clusters are condensed in the sodium flame before contact is made with the rapidly lengthening chains of U_3O_8. Apparently, there is never an opportunity for liquid droplets of the vapor condensation products to form primary particles simultaneously and thereby result in an interspersed linkage between each in a heterogeneous chain. Therefore, it is most likely that a primary sodium particle is entrapped on a short U_3O_8 chain and then becomes a nucleus for continued growth into a 1- to 3-μ cluster, while the U_3O_8 continues to increase in size to a self-preserving limit before settling.

2.3.3 Characterization of mixed-oxide in run PT-33

In Fig. 11, the deposition rates of both components of the aerosol mixture are shown as determined both by plotting the direct weights as well as the analytically determined concentrations of uranium and sodium in each filter sample. The relatively constant ratio of uranium to sodium is apparent; however, the limits of accuracy of the lower concentration values should be considered. Also note (Table 7) that the ratio of uranium to sodium tends to increase with respect to time, although this is a relatively small effect.

The ratio of uranium to sodium can also be determined by detailed analysis of the size distribution data from both the spiral centrifuge and the cascade impactors. Figure 12, a histogram of the centrifuge data, shows both curves to be nearly symmetrical. There is, therefore, little reason to conclude that a significant fraction of the sodium is present as separate particles in the mixture.

Examination of the TEM photomicrographs (Fig. 13 for Run 28 and Fig. 14 for Run 33) also fails to show any unattached sodium. The low-magnification view clearly distinguishes the sodium clusters, and from

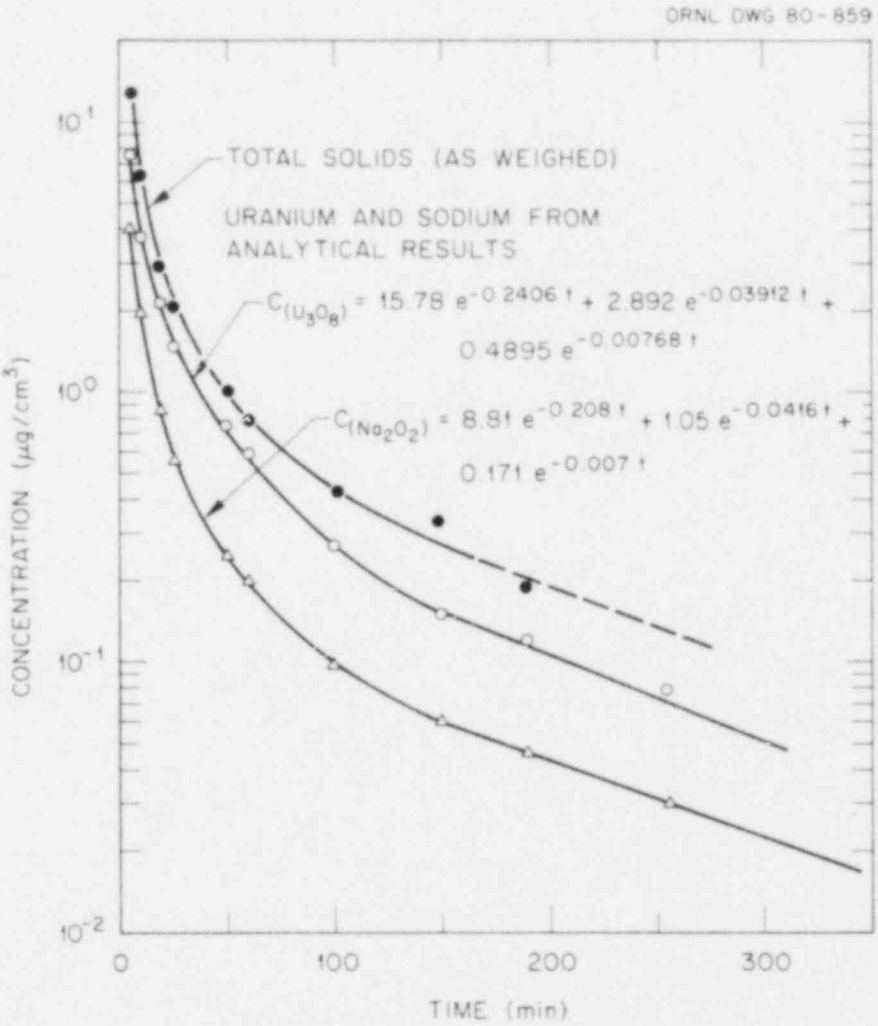

Fig. 11. Deposition rates for mixed oxides in Run PT-33.

Table 7. Calculated ratios of uranium to sodium in mixed oxide[a] in Run PT-33 at various times from end of burn period

Sample No.	Impactor data		Filter samples		Centrifuge foils	
	Time of measurement (min)	U/Na ratio	Time of measurement (min)	U/Na ratio	Time of measurement (min)	U/Na ratio
1	14	2.05	10	2.0	10	2.05
2	64	2.45	90	2.5	90	2.19
3	130	2.79	245	2.3	245	2.36
4	282	2.43				

[a]Calculated as mass ratio of $U_3O_8/Na_2O \cdot H_2O$.

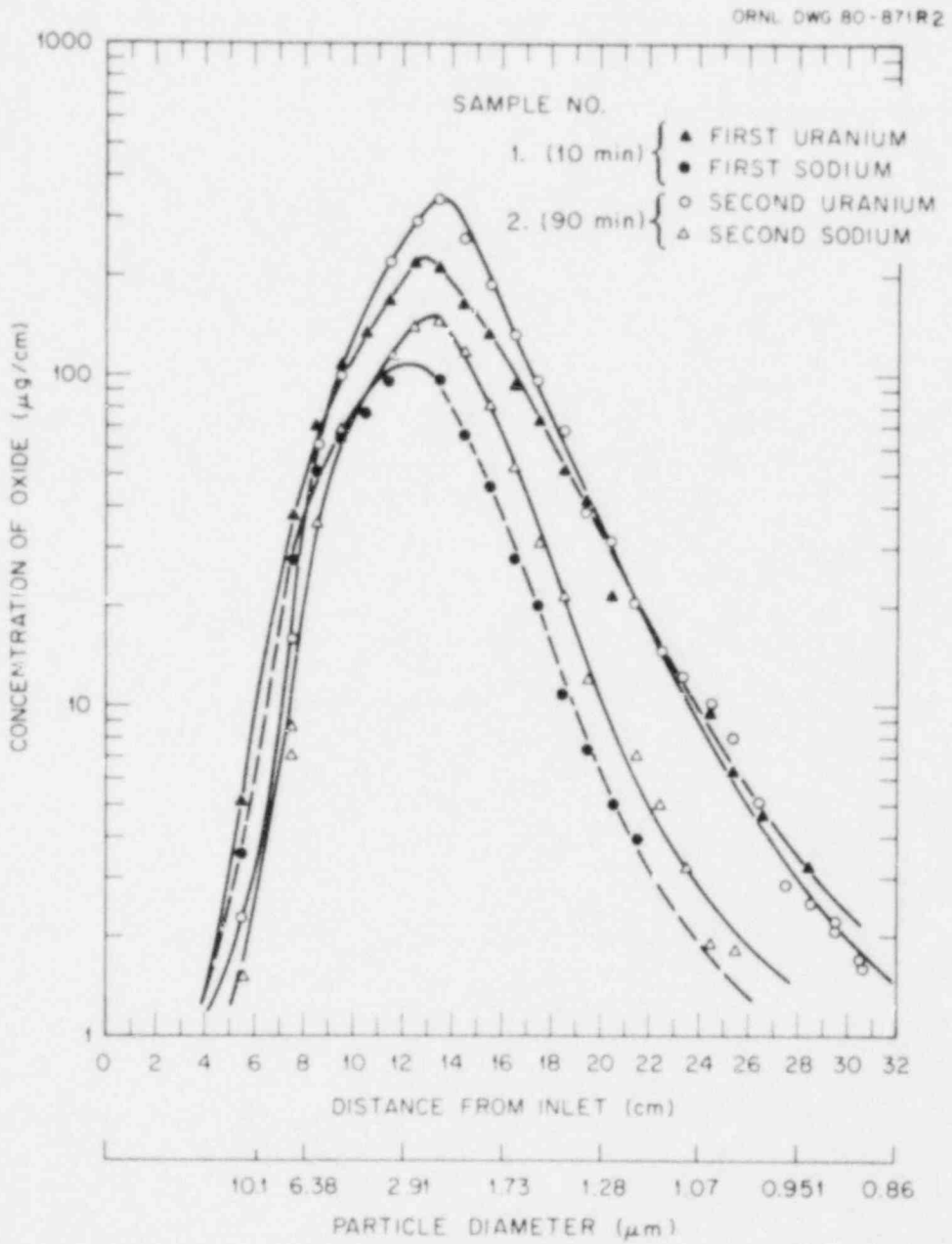

Fig. 12. Size distributions of uranium and sodium mixed oxide aerosols measured by spiral centrifuge for Run PT-33.

the high-magnification view a small amount of translucence in the clusters suggests that the aggregates are formed as a number of spheres partially fused together into a high-density compact.

Plans have been made to investigate a new technique using an electron microprobe with which individual clusters may be identified by induced x-ray fluorescence for their individual content of both sodium and uranium.

Fig. 13. Photomicrographs showing Na_2O_2 cluster aggregates on U_3O_8 chain agglomerates for Run PT-28. (Original reduced 20%)

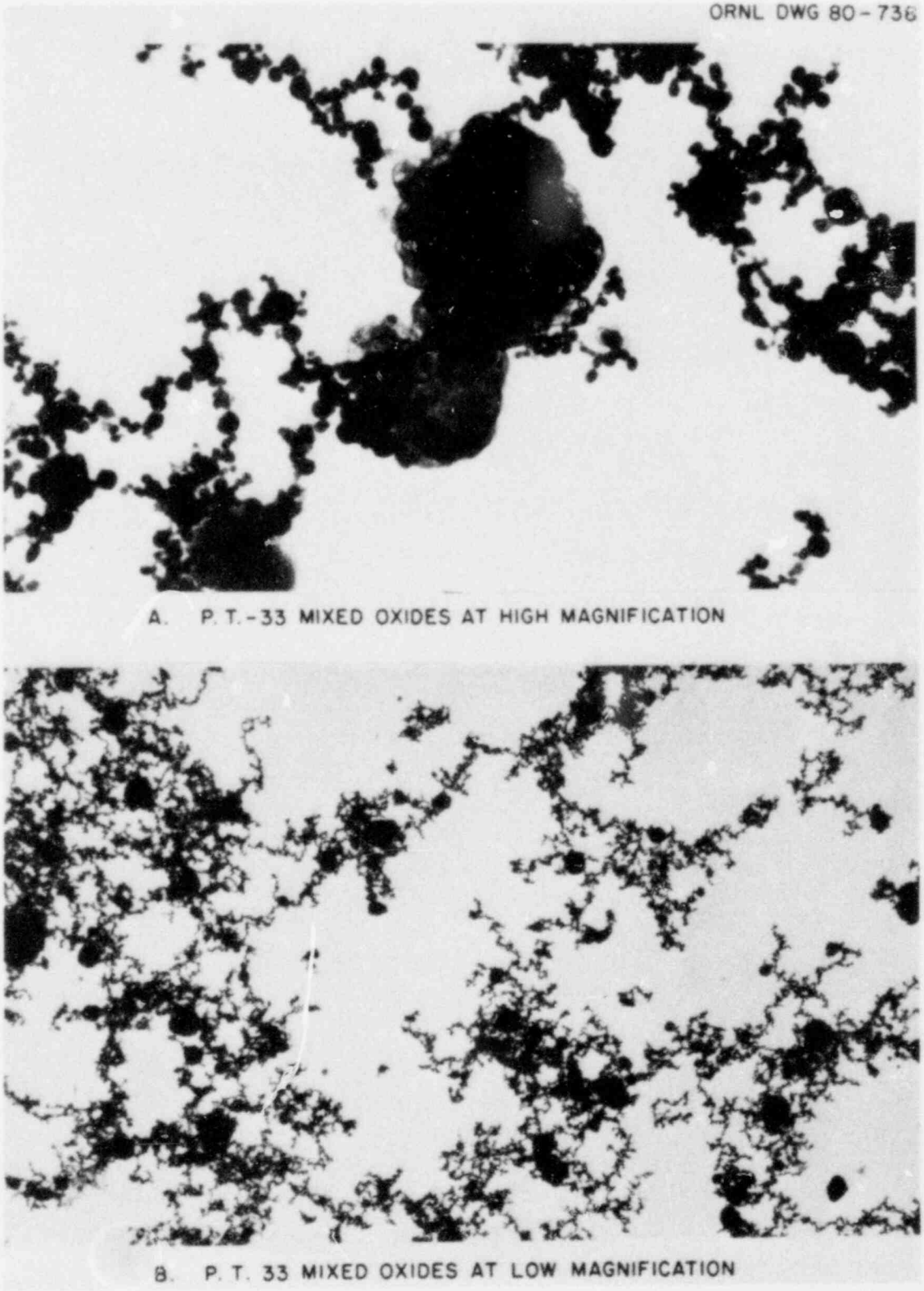

Fig. 14. Photomicrographs showing Na_2O_2 cluster aggregates on U_3O_8 chain agglomerates for Run PT-33. (*a*) PT-33 mixed oxides at high magnification; (*b*) PT-33 mixed oxides at low magnification. (Original reduced 13%)

3. ANALYTICAL PROGRAM

M. L. Tobias

3.1 Simplified Methods for Calculating Bubble-Liquid Interface Temperatures in Analysis of FAST Experiments

3.1.1 Introduction

While it is possible to construct finite difference schemes for the calculation of transient conduction heat transfer at the bubble-liquid interface, these will offer difficulties from the standpoints of running time, numerical stability, and code size. Since the heat conduction loss term is relatively small and therefore probably not crucial to the accuracy of final results, simpler methods of calculation seem called for. We will discuss an approach based on the integral balance method of Goodman.

3.1.2 Goodman's integral balance method[6,7]

The core of the procedure consists of the following assumptions (Fig. 15):

1. A form for the temperature distribution is assumed.
2. The heat flow integral over a time interval is set equal to the heat absorbed in an interval δ. The interval δ is a function of time.
3. Initially, δ is assumed zero. For all distances from the surface greater than δ, no temperature effects occur, nor is there any heat flow beyond δ.

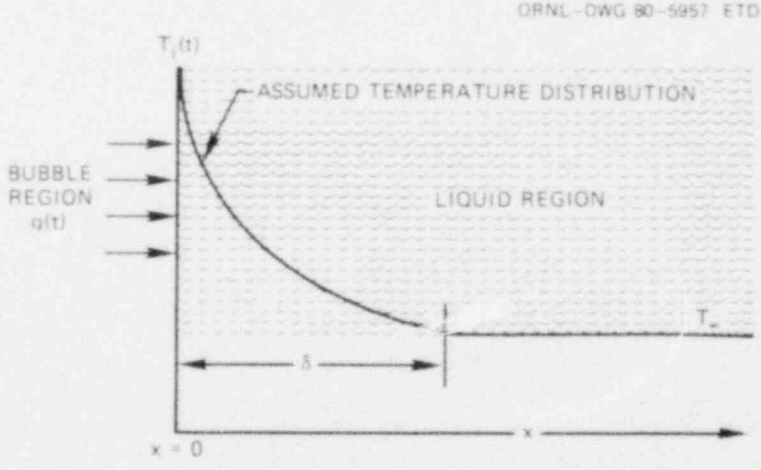

Fig. 15. Schematic drawing illustrating integral balance method as applied to FAST analysis. Heat flux at interface q(t) a function of time. T_∞ is initial liquid region temperature, constant for $x > \delta$, where δ is also a function of time.

The obvious boundary conditions can be used. In addition one may specify, if desired, that the heat conduction equation, $k\nabla^2 T = c\rho\partial T/\partial t$, is to be satisfied at the boundaries or in the mean over the interval $0 \leq x \leq \delta$. The specifics of each application are largely up to the user's judgment. The method leads to simple closed-form results. (Some comparisons with analytical results are exhibited in Ref. 7).

Assuming a parabolic temperature distribution and slab geometry, it is obvious that the form

$$T(x,t) - T_\infty = a(\delta - x) + b(\delta - x)^2 \quad 0 < x < \delta \tag{1}$$

will satisfy the requirement that $T(x,t) = T_\infty$ at $x = \delta$. At all times,

$$-k \left.\frac{dT}{dx}\right|_{x=0} = q(t) .$$

Therefore,

$$-k[-a - 2b\delta] = q(t) . \tag{2}$$

The integral balance condition is

$$\int_0^\delta c\rho[T(x,t) - T_\infty]\, dx = \int_0^t q(t')dt' , \tag{3}$$

where the right side is the total heat entering the liquid region from time 0 to t, while the left side is the enthalpy of the region from 0 to δ.

$$-c\rho \left[\frac{a}{2}(\delta - x)^2 + \frac{b(\delta - x)^3}{3}\right] \Bigg|_0^\delta = \overline{q}t \tag{4}$$

or

$$c\rho\left(\frac{a\delta^2}{2} + \frac{b\delta^3}{3}\right) = \overline{q}t = \int_0^t q(t')dt' . \tag{5}$$

Suppose we further require that $-k\, dT/dx = 0$ at $x = \delta$, on the ground that there is no heat loss at this point. Since

$$\frac{\partial T}{\partial X} = -a + 2b(\delta - x) \tag{6}$$

so that

$$\frac{\partial T}{\partial X} = -a = 0 \text{ at } x = \delta, \text{ then } a = 0 . \tag{7}$$

We have further that

$$-k[-a - 2b\delta] = + 2kb\delta = q(t) \tag{8}$$

or

$$b = q(t)/2k\delta .$$

The integral balance condition now reads

$$\frac{c\rho b\delta^3}{3} = \left(\frac{c\rho\delta^3}{3}\right)\left(\frac{q}{2k\delta}\right) = \frac{q\delta^2}{6\alpha} = \overline{q}t . \tag{9}$$

Therefore,

$$\delta = \sqrt{\frac{\overline{q}}{q}\, 6\alpha t} , \tag{10}$$

where $\alpha \equiv k/c\rho$. The interface temperature $T(x = 0,t)$ is found to be

$$T(0,t) - T_\infty = \frac{q\delta}{2k} = \sqrt{\left(q\overline{q}\right)\left(\frac{3\alpha t}{2}\right)} . \tag{11}$$

The validity of this result may be examined by comparison with known solutions. First, if q is constant with time we have

$$T(0,t) - T_\infty = \frac{q}{k}\sqrt{\frac{3}{2}\,\alpha t} \cong 1.225\,\frac{q}{k}\sqrt{\alpha t} . \tag{12}$$

This is to be compared with the well-known analytical result

$$T(0,t) - T_\infty = \frac{q}{k}\sqrt{\frac{4}{\pi}\,\alpha t} \cong 1.128\,\frac{q}{k}\sqrt{\alpha t} . \tag{13}$$

The integral-balance method therefore gives a factor which is about 9% too large. As Goodman has shown,[6] this result may be improved by use of a cubic representation in which the additional assumption is made that

$$\partial^2 T/\partial x^2\big]_{x=\delta} = 0 \ . \tag{14}$$

The result then becomes $T(0,t) - T_\infty = \sqrt{4/3\alpha t \ q\bar{q}}$, which becomes 1.155 $q\sqrt{\alpha t}$ for constant q. This is only 2.4% too high. A variety of other assumptions and suppositions might be made, not necessarily leading to improved accuracy. An obvious improvement would be to use the formula

$$T(0,t) - T_\infty = 1/k \sqrt{(4/\pi) \ q\bar{q}\alpha t} \ , \tag{15}$$

which will fit the analytical answer for constant q. This expression, however, has to be used with a certain amount of caution. If, for example, the instantaneous value q should be zero, then T(0,t) is calculated equal to T_∞, an incorrect result. In the present application, q will be of a monotonically changing character, and when q becomes small, we may expect T(0,t) to approach T_∞.

Suppose that q is a linear function of time, $q = 7000 - 3500t$, the coefficients being reasonably typical of FAST experimental conditions. The exact solution would be

$$T(0,t) - T_\infty = \frac{1}{k}\sqrt{\frac{4\alpha t}{\pi}} \left(q + \frac{1}{3} \cdot 3500t\right) \quad 0 < t < 2 \ , \tag{16}$$

while the integral balance method would give

$$T(0,t) - T_\infty = \frac{1}{k}\sqrt{\frac{4\alpha t}{\pi}} \left[q \left(7000 - \frac{3500}{2} \ t\right)\right]^{1/2} \ . \tag{17}$$

Similarly, if q is a parabolic function of time $7000 \ (1 - t/2)^2$, more typical in form of FAST conditions, the exact solution is

$$T(0,t) - T_\infty = \frac{1}{k} \sqrt{\frac{4\alpha t}{\pi}} \left[q + \left(\frac{7000}{3}\right)\left(\frac{t - 7t^2}{20}\right)\right], \tag{18}$$

while the integral-balance method gives

$$T(0,t) - T_\infty = \frac{1}{k} \sqrt{\frac{4\alpha t}{\pi}} \left[q \ (7000)\left(1 - \frac{t}{2} + \frac{t^2}{12}\right)\right] \ . \tag{19}$$

The solutions therefore differ in the bracketed factors compared in Table 8.

Clearly, the integral balance result deviates more and more strongly from the exact result as time increases until finally it is 100% off at 2 s. While the $\sqrt{q\bar{q}}$ formalism could be used because the largest errors occur late in time where effects are small, the error comparison suggests that improvements are needed to reduce the error at low values of q.

Table 8. Comparison of integral balance method with exact solution for interface temperature for surface heat flux linear or parabolic in time

Time (s)	Factors for q linear in time			Factors for q parabolic in time		
	Exact solution	Integral balance method	Difference (%)	Exact solution	Integral balance method	Difference (%)
0	7000	7000	0.0	7000	7000	0.0
0.5	5833	5671	−2.8	4900	4610	−5.9
1.0	4667	4287	−8.1	3267	2673	−18.2
1.5	3500	2767	−20.9	2100	1158	−44.8
2.0	2333	0.0	−100	1400	0.0	−100

REFERENCES

1. A. L. Wright and A. M. Smith, *Updated Work Plan for the FAST/CRI-III Fuel Vaporization and Transport Experiments*, ORNL/NUREG/TM-326 (October 1979).

2. T. S. Kress and M. L. Tobias, *LMFBR Aerosol Release and Transport Program Quarterly Progress Report for October–December 1979*, ORNL/NUREG/TM-391 (June 1980).

3. T. S. Kress and J. T. Han, *LMFBR Aerosol Release and Transport Program Quarterly Progress Report for January–March 1979*, ORNL/NUREG/TM-329 (August 1979).

4. T. S. Kress and A. L. Wright, *LMFBR Aerosol Release and Transport Program Quarterly Progress Report for April–June 1979*, ORNL/NUREG/TM-354 (January 1980).

5. T. S. Kress, *LMFBR Aerosol Release and Transport Program Quarterly Progress Report for July–September 1979*, ORNL/NUREG/TM-376 (April 1980).

6. T. R. Goodman, *Advances in Heat Transfer*, Vol. 1, pp. 52–122, Academic Press, New York, 1964.

7. D. Langford, "The Heat Balance Integral Method," *Intl. J. Heat Mass Transfer* 16, 2424–28 (1973).

NUREG/CR-1790
ORNL/NUREG/TM-416
Dist. Category R7

Internal Distribution

1. R. E. Adams
2. M. Bender
3. H. W. Bertini
4. J. R. Buchanan
5. W. B. Cottrell
6. G. F. Flanagan
7. M. H. Fontana
8. U. Gat
9. H. W. Hoffman
10-14. T. S. Kress
15. R. E. MacPherson
16. A. P. Malinauskas
17. F. R. Mynatt
18. G. W. Parker
19. P. Patriarca
20-21. J. L. Rich
22. J. M. Rochelle
23. A. M. Smith
24. I. Spiewak
25. A. L. Sutton, Jr.
26. D. G. Thomas
27-28. M. L. Tobias
29. H. E. Trammell
30. D. B. Trauger
31. J. L. Wantland
32. J. A. Stevens
33. R. P. Wichner
34. G. D. Whitman
35. A. L. Wright
36. ORNL Patent Office
37. Central Research Library
38. Document Reference Section
39-40. Laboratory Records Department
41. Laboratory Records (RC)

External Distribution

42. M. Silberberg, Chief, Experimental Fast Reactor Safety Research Branch, Division of Reactor Safety Research, Nuclear Regulatory Commission, Washington, DC 20555
43. R. Sherry, Division of Reactor Safety Research, Nuclear Regulatory Commission, Washington, DC 20555
44. Demetrios Basdekas, Division of Reactor Safety Research, Nuclear Regulatory Commission, Washington, DC 20555
45-48. Director, Office of Nuclear Regulatory Research, Nuclear Regulatory Commission, Washington, DC 20555
49. Office of Assistant Manager for Energy Research and Development, DOE, ORO, Oak Ridge, TN 37830
50-51. Technical Information Center, DOE, Oak Ridge, TN 37830
52-431. Given distribution as shown in category R7 (NTIS-10)